

Critical length scales for chemical heterogeneity at Cu/Nb 3D interfaces by atom probe tomography



Zezhou Li ^{a,1}, Justin Y. Cheng ^{a,1}, Jonathan D. Poplawsky ^{b,*}, Shuzhi Xu ^d, Jon K. Baldwin ^c, Irene J. Beyerlein ^{d,e}, Nathan A. Mara ^{a,*}

^a Department of Chemical Engineering and Materials Science, University of Minnesota, Minneapolis, MN 55455, United States

^b Center for Nanophase Materials Sciences, Oak Ridge National Laboratory, Oak Ridge, TN 37831, United States

^c Center for Integrated Nanotechnologies, MPA-CINT, Los Alamos National Laboratory, Los Alamos, NM 87545, United States

^d Department of Mechanical Engineering, University of California, Santa Barbara, CA 93106, United States

^e Materials Department, University of California, Santa Barbara, CA 93106, United States

ARTICLE INFO

Keywords:

3D interfaces
Cu/Nb nanolaminates
Physical vapor deposition
Atom probe tomography
Surface diffusion

ABSTRACT

Cu/Nb nanocomposites containing sharp, two-dimensional (2D) interfaces have outstanding strength but limited deformability. In contrast, Cu/Nb with three dimensional (3D) biphase interfaces exhibiting crystallographic, topological, and chemical variations in all spatial dimensions overcomes this limitation by simultaneously enhancing material strength and deformability. While structural characterization of 3D interfaces has been performed to understand their mechanical behavior, three dimensional chemical characterization of such interfaces is lacking. In this work we quantify the local chemistry of 3D interfaces in Cu/Nb nanocomposites using atom probe tomography (APT). Our analysis demonstrates chemical heterogeneities along all spatial dimensions in 3D interfaces, establishes the length scale of such features, and quantifies the morphology of 3D interfaces. 3D interface heterogeneities form by surface diffusion during physical vapor deposition (PVD), suggesting that deposition parameters can be used to control interface structure and provide unique ways to explore processing-structure-property relationships in interface-dominated nanocomposites.

Recently, the metallurgy community has paid much attention to how interface structure produces outstanding mechanical performance in nanocrystalline alloys and composites [1–4]. However, we have only begun to explore the possibility of manipulating atomic-level interfacial structures to enhance mechanical properties [5–7]. Many studies use layered bimetal nanocomposites with layer thicknesses less than 100 nm to study interface-dominated deformation; Cu/Nb nanocomposites with chemically sharp two-dimensional (2D) interfaces [8], called 2D Cu/Nb, are a popular choice. Heterophase interfaces in these materials are dominated by Nishiyama-Wasserman and Kurdjumov-Sachs type interfaces whose local atomic structures are synthesized controllably and repeatedly to confer desirable properties, such as high strength and

ductility [9,10]. At a layer thickness of 5 nm, 2D Cu/Nb can achieve a high strength of 2.4 GPa and deforms uniformly up to 16% strain when compressed normal to the interfaces [9]. The atomic structure and corresponding low shear strength of 2D Cu/Nb interfaces produce this behavior; dislocations impinging on them spread and become trapped before transmitting across such interfaces [10–12]. Although 2D Cu/Nb is promising for achieving high strength, shear banding limits its plasticity. To combat this limitation and elucidate the physics underlying superior deformability, we study physical vapor-deposited (PVD) Cu/Nb nanolaminates containing 3D interfaces with crystallographic, topological, and chemical heterogeneities in all spatial dimensions; these nanocomposites are called 3D Cu/Nb. 3D Cu/Nb is stronger and more

This manuscript has been authored by UT-Battelle, LLC under Contract No. DE-AC05-00OR22725 with the U.S. Department of Energy. The United States Government retains and the publisher, by accepting the article for publication, acknowledges that the United States Government retains a non-exclusive, paid-up, irrevocable, world-wide license to publish or reproduce the published form of this manuscript, or allow others to do so, for United States Government purposes. The Department of Energy will provide public access to these results of federally sponsored research in accordance with the DOE Public Access Plan (<http://energy.gov/downloads/doe-public-access-plan>).

* Corresponding authors.

E-mail addresses: poplawskyjd@ornl.gov (J.D. Poplawsky), mara@umn.edu (N.A. Mara).

¹ These authors contributed equally to this work.

deformable than 2D Cu/Nb [13–15], but the structure of 3D interfaces and its implications on the physics of mechanical behavior are not fully understood.

Although it is known that 3D interfaces are crystallographically heterogeneous on the length scale of a few nm, the nature of chemical heterogeneity in 3D interfaces remains unclear. Crystallographic heterogeneities in all spatial dimensions found via high resolution transmission electron microscopy (HRTEM) suggest that substantial chemical rearrangement occurs during 3D interface synthesis, yet these interfaces are not chemically heterogeneous in all spatial dimensions under scanning transmission electron microscopy-energy dispersive spectroscopy (STEM-EDS) [13]. TEM methods, which project volumetric information onto an image plane, are fundamentally limited from resolving this contradiction [16]. To address these limitations, we use atom probe tomography (APT) to characterize chemical heterogeneities in 3D

Cu/Nb interfaces. APT combines time-of-flight mass spectrometry with a three-dimensional projection microscope to map the 3D distribution of elements with sub-nm resolution and <10 ppm chemical sensitivity. Unfortunately, spatial resolution is limited to a few nm at interfaces due to reconstruction errors and heterogeneous field evaporation [17–19]. In this work, APT is used to quantify key 3D interface microstructural metrics: the length scale associated with chemical heterogeneities, the variation of chemical gradients in the through-thickness and in-plane directions as a function of position, and interface thickness. Here, a chemical heterogeneity is defined as a region that has divergent chemistry from adjacent regions in an in-interface plane direction, or a divergent chemical gradient from adjacent regions in the interface plane normal direction. We also find that chemical heterogeneities are correlated to geometric features in 3D interfaces, suggesting a surface-diffusion based formation mechanism for chemical

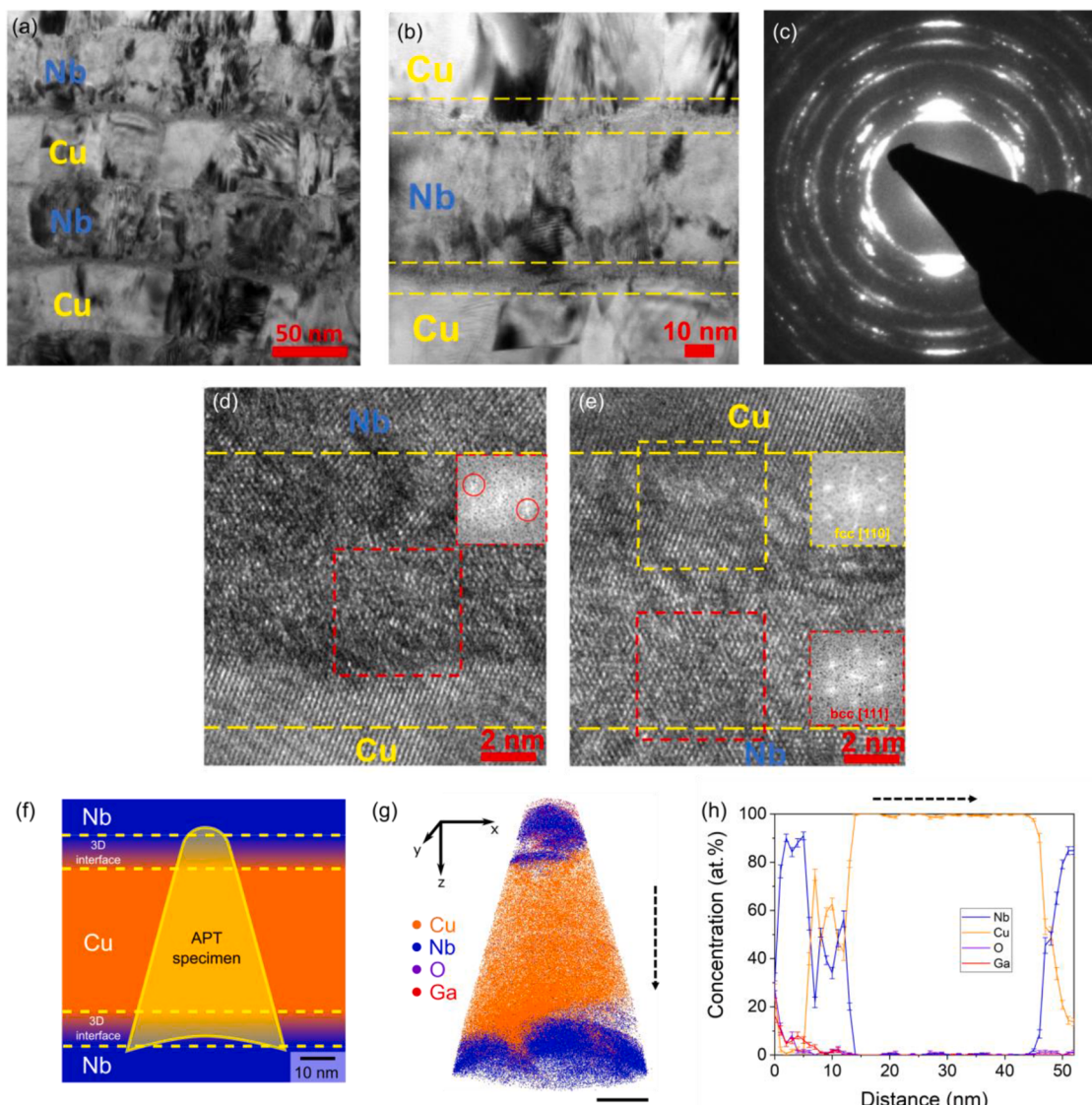


Fig. 1. (a-b) Bright-field TEM images of 40–10 Cu/Nb, demonstrating the presence of 3D interfaces between pure Cu and Nb layers. (c) Selected area diffraction pattern taken from (a). (d) HRTEM image of an 3D interface containing both disordered and crystalline structures, as shown in the fast Fourier transform (FFT) inset. (e) HRTEM image of a Cu/Nb interface with a Kurdjumov-Sachs (K-S) orientation relationship, demonstrated by the FFT inset. (f) A schematic showing the region from which an APT needle was extracted from 40–10 Cu/Nb. The bottom of this region is drawn with a missing hemispherical region to represent missing data due to evaporation aberrations. (g) APT map of 40–10 Cu/Nb containing one layer of pure Cu and two 3D interfaces, one each at the top and bottom of the needle. (h) A chemical profile extracted from a region of interest (ROI) with 5 nm diameter and 1 nm bin size from the center of the needle in (g). The dependent axis in (h) corresponds to the direction indicated by the dotted arrow in (g). Error bars in plots represent one interval of standard error due to counting statistics of atoms included in the ROI [17]. Significant amounts of Ga are found at the tip of the needle due to damage from FIB milling, and O is found at the same region due to oxidation during sample transfer from the FIB to the LEAP. Scale bars in (f-g) represent 10 nm.

heterogeneities in PVD-synthesized 3D interfaces.

Material synthesis for this work comprised DC magnetron sputtering of Cu/Nb nanolaminates containing 3D interfaces. Cu and Nb target powers were linearly modulated between deposition of pure Cu and Nb layers to form 3D interfaces in the same manner as prior work [13]. Nomenclature of specimens is based on nominal thickness of pure Cu and Nb layers and 3D interface thickness expressed in nm, e.g., 40–10 Cu/Nb represents a composite with 40 nm thick pure Cu and Nb layers and 10 nm thick 3D interfaces in between pure layers. We fabricated APT needles from 40–10 Cu/Nb using a Thermo Fisher Nova 200 FIB/SEM. 3D interfaces were targeted using standard liftout and sharpening techniques [20]. A CAMECA local electrode atom probe (LEAP 4000X HR) was used for APT experiments. Specimens were run in laser mode with a 200 kHz pulse repetition rate, 0.5% detection rate, 30 K base temperature, and 30–60 pJ laser energy. APT data were reconstructed and analyzed using CAMECA's integrated visualization and analysis software (IVAS) 3.8.6. Cross-sectional TEM micrographs were also taken of 40–10 Cu/Nb. Lamellae were lifted out of 40–10 Cu/Nb thin films using an FEI Helios NanoLab G4 FIB/SEM and imaged in conventional TEM at normal and high-resolution magnification using a Thermo Fisher Talos FX200 at 200 keV.

TEM and APT data show that 3D interfaces are non-planar and contain structural and chemical heterogeneities in all spatial dimensions, as seen in Fig. 1. TEM diffraction contrast in Figure 1(a-b) shows that disordered regions in the 3D Cu-Nb interfaces appear wavy. The selected area diffraction pattern in Figure 1(c) demonstrates strong epitaxy between Cu and Nb layers. HRTEM characterization in Fig. 1(d-e) shows that 3D interfaces contain a range of crystallographic order. Some regions contain disordered and crystalline regions as seen in Fig. 1(d), while others nearly resemble 2D interfaces as seen in Fig. 1(e). An APT needle was extracted as depicted in Fig. 1(f) to produce the 3D chemical map in Fig. 1(g) and the chemical profile in Fig. 1(h). Fig. 1(g)

h) demonstrate that 3D interfaces possess in-plane chemical heterogeneities and non-linear through-thickness chemical gradients despite linear ramping of target powers during the deposition process. The region of interest (ROI) parameters used for Fig. 1(h) and other figures in this work were chosen to include sufficient atoms per ROI slice to ensure adequate counting statistics [17], but as discussed in Figs. S1 and S3 are of limited enough size to resolve chemical features in 3D interfaces. The mass spectrum from this APT needle can be found in Fig. S2. The chemistry of 3D interfaces can be further quantified by considering composition and chemical gradients at different lateral positions in the through-thickness and in-plane directions.

Through-thickness APT characterization of 3D interfaces demonstrates differences in chemical gradients as a function of lateral position, allows measurement of their thickness independently of TEM data, and establishes a length scale for chemical heterogeneity in 3D interfaces. To demonstrate, we extract chemical profiles normal to 3D interfaces along cylindrical ROIs at the top and bottom of the needle as depicted in Fig. 2 (a,d). At the top of the APT needle, Fig. 2(b) shows a sigmoidal chemical gradient, typical of an interface, while Fig. 2(c) shows a metastable composition between the Cu and Nb layers comprised of 50 at.% Cu and 40 at.% Nb. Similarly at the bottom of the needle, the interfacial chemical gradient in Fig. 2(e) is sigmoidal, while the 3D interface contains a metastable composition between the Cu and Nb layers in Fig. 2(f). The metastable compositions in Fig. 2(c,f) span about 5 nm in the interface normal direction. The average thickness of the 3D interface at the top of the needle is 8.7 ± 0.9 nm based on 13 measurements (see Figure S3 for details of measurement). Thicknesses were not measured at the bottom of the needle because of missing data in a hemispherical region there due to specimen fracture during the APT experiment. For 3D interface thickness measurements, we use threshold values of 90 at.% Cu and 10 at.% Cu to define the boundaries of Cu and Nb pure layers, respectively. These values correspond to a commonly used criterion in

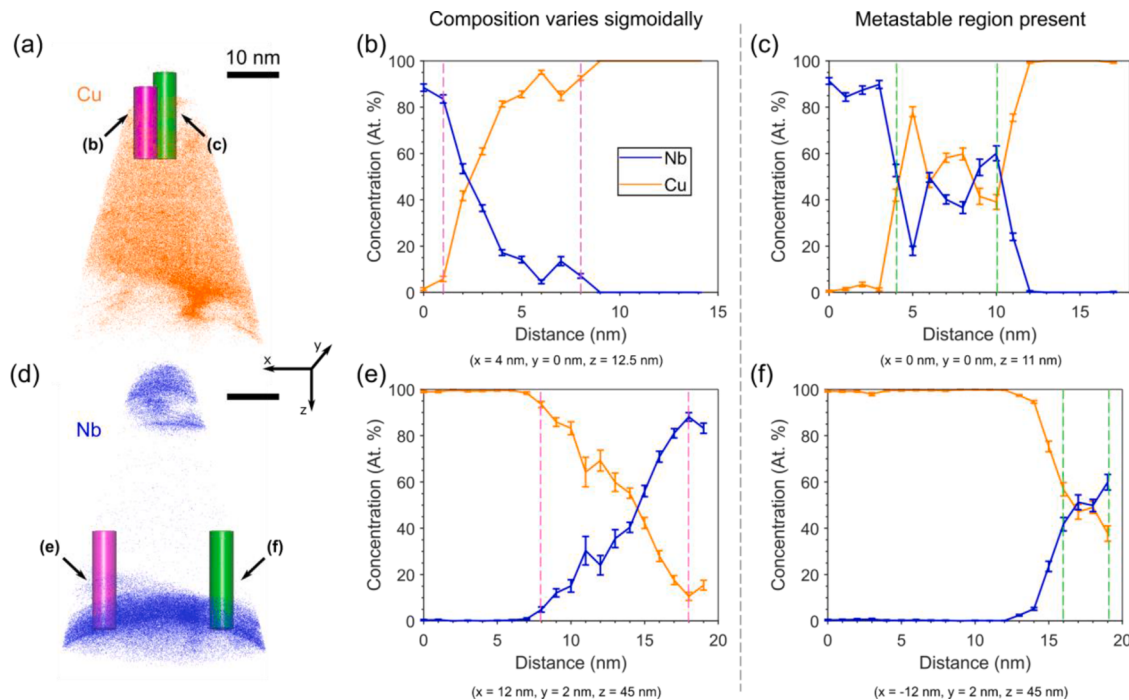


Fig. 2. (a) An APT Cu map on which ROIs 5 nm wide are extracted to produce chemical profiles with bin width of 1 nm shown in (b-c). ROIs are denoted by magenta and green bars embedded in the needle. These profiles are taken along the z direction starting at the top of the APT needle. Composition varies smoothly in the 3D interface at position (b). This smooth chemical gradation is indicated by magenta dotted lines. In contrast, chemically intermixed regions are present in the 3D interface at (c). This phenomenon is indicated by green dotted lines in (c). (d) An APT Nb map of the same sample as in (a), on which ROIs with the same parameters as (a) are extracted to produce chemical profiles shown in (e) and (f). Similarly, as seen in (b) and (c), (e) contains a smooth chemical gradient, while (f) displays a chemically intermixed region with constant composition. Error bars for (b-c, e-f) are the same as defined in Figure 1(h). Axes defining the frame of reference illustrated in (a) are the same as in (d). Scale bars in (a,d) represent 10 nm.

APT literature that sets diffuse interface boundaries at 90% and 10% of plateau concentrations of a given species [21,22]. APT interface thickness measurements are slightly lower than interface thickness measurements made via STEM-EDS (10.6 ± 2.1 nm) [13]. This is to be expected, as interface waviness is averaged out using STEM-EDS and the criterion for interface boundary used in Ref. [13] was different; maximum and minimum values of Nb were used to define interface boundaries in that study. APT interface thickness measures are substantially greater than those made via HRTEM (4–6 nm) [15], indicating that chemical and structural methods of 3D interface characterization are distinct and represent independent and complementary information.

Lateral heterogeneities are found in 3D interfaces of similar size to those observed in the through-thickness direction. In-plane chemical gradients are a function of lateral position similarly to through-thickness gradients. This can be seen in x-y sections of Cu concentration maps taken at various values of z. All maps presented in this work are created using a voxel size of 1 nm x 1 nm x 1 nm and a delocalization of 3 nm x 3 nm x 3 nm. Sections depicted in Fig. 3(a) span a region between the middle of a pure Cu layer and the middle of a 3D interface. A Cu-rich

finger-like region measuring 40 nm and 10 nm in the x and y directions, respectively, is found at $x = 52$ nm. Chemically segregated regions are quantified in via chemical profiles in Fig. 3(b-c) along the x and y directions. These profiles show that the length scales of lateral chemical features in the 3D interface characterized are 7 and 14 nm for the x and y directions, respectively. Local magnification may skew these values, but such artefacts skew size measurements of chemical features by a factor of 2–5 and are accurate to well within an order of magnitude [19]. This is supported by the repeatability of APT results demonstrated on another 40–10 specimen in Fig. S4. This analysis suggests that geometric features in the x-y directions in 3D interfaces are correlated to chemical heterogeneities. We shall show the same is true in the y-z and x-z directions.

3D interface isoconcentration surfaces (isosurfaces) and chemical heat maps demonstrate the relationship between interface geometry and chemical heterogeneities in the y-z and x-z directions of 3D interfaces in Fig. 4. 50 at.% Cu isosurfaces representative of interface geometry are presented from two different views in Fig. 4(a,f). These figures show that interface curvature varies laterally in 3D interfaces. To isolate and

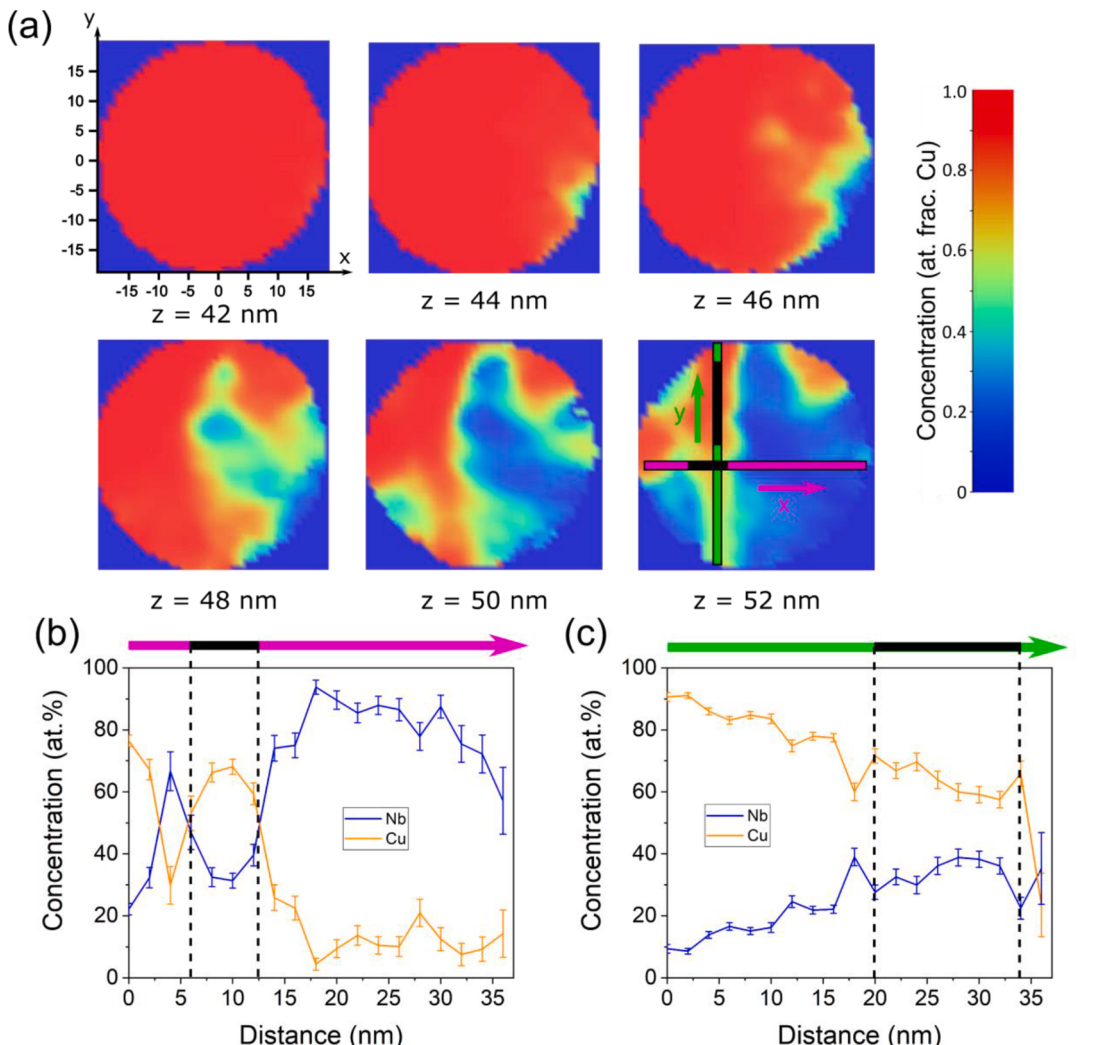


Fig. 3. (a) Cross-sectional chemical heat maps at z positions spanning from the middle of a pure Cu layer to the middle of a 3D interface. Slices are 4 nm thick, except for $z = 52$ nm, which is 2 nm due its proximity to the limit of data at the bottom of the needle. Reference axes depicted at $z = 42$ nm are the same as in the rest of the slices and are in nm. Profiles are extracted from $z = 52$ nm with ROI width of 2 nm and bin width of 2 nm to demonstrate chemically segregated regions in the (b) x and (c) y directions. ROI width is increased and bin width is decreased relative to other ROIs in this work to ensure good sampling while keeping the ROI within the bounds of the $z = 52$ nm slice. The x and y profiles are aligned with the magenta and green lines in (a) at $z = 52$ nm, respectively. The solid black lines found in (a) at $z = 52$ nm, (b), and (c) indicate chemically segregated regions along respective chemical profiles. (b) depicts a chemically segregated region that is ~7 nm wide in the x direction, while (c) depicts a chemically segregated region that is ~14 nm wide in the y direction. Error bars depict one interval of standard error.

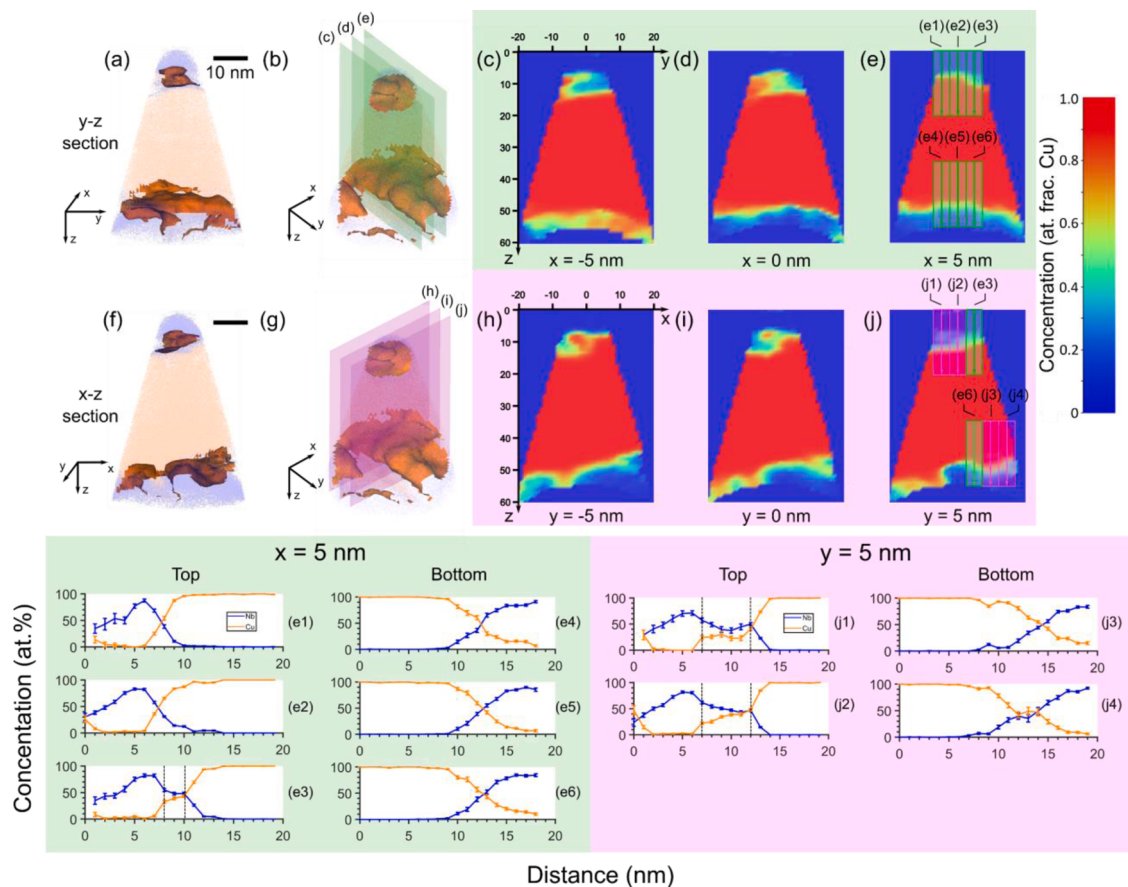


Fig. 4. Iso-concentration surfaces depicted in orange, taken at 50 at.% Cu when viewed parallel to the (a) x axis and (f) y axis. Surfaces are superimposed on atom maps using the same color key as in Figure 1(g) to depict their location in the needle. Cu concentration maps are presented for 5 nm-thick cross sections taken from the regions depicted in (b,g), which show the same isometric view of the 50 at.% Cu isosurfaces. These maps comprise (c-e) y-z sections and (h-j) x-z sections at the x and y axes indicated. Chemical profiles extracted from the regions indicated by boxed arrows in (e,j) are shown in (e1-e6,j1-j4). Dotted lines highlight regions with metastable compositions in (e3,j1-j2,j4). Scale bars are shared between (a-b,f-g), while reference axes are shared between (c-e,h-j). All scale bars are 10 nm, and reference axes are in nm. Legends in (e1) and (j1) are shared with the other chemical profiles. Error bars in profiles represent one interval of standard error. Note that (e) and (j) overlap partially, meaning that profiles placed at $x = 5$ nm in (j) would be duplicates of (e3,e6), which are also at $x = 5$ nm, $y = 5$ nm.

visualize interface geometry at specific regions of the APT needle, we extracted 2D Cu chemical concentration maps from the planes indicated in Fig. 4(b,g) and show them in Fig. 4(c-e,h-j). Some parts of the 3D interface are flatter than others; the top and bottom interfaces in Fig. 4(e) are relatively flat, while in Fig. 4(j), the top interface is diffuse in the z direction and the bottom interface contains a large excursion near $x = 0$ nm. Chemical profiles were extracted from these different interface types to determine if interface geometry is correlated with chemical heterogeneity. Profiles were extracted in the indicated regions in Fig. 4(e,j) to produce Fig. 4(e1-e6,j1-j6). The chemical profiles reveal regions with a sigmoidal-like chemical gradient typical of a interface in Fig. 4(e1-e2,e4-e6,j3-j4) and regions that have metastable composition between the Cu and Nb layers in Fig. 4(e3,j1-j2). Since regions with metastable compositions were found in both Fig. 4(e) and (j), we find that 3D interfaces contain chemical heterogeneities regardless of local interface geometry. These heterogeneities may be nanoprecipitates of distinct chemical composition compared to adjacent material. The presence of these regions provides important clues regarding their mechanism of formation.

Geometrical features and associated chemical heterogeneities in 3D interfaces are likely formed by surface diffusion during PVD. It is well known that surface diffusion is appreciable during deposition processes and can dominate microstructure formation under a wide range of deposition conditions [23–27]. A schematic depicting the formation mechanism of a Cu-rich region is found in Fig. 5(a,b) and assumes

Stranski-Krastanov-like film growth [28]. Based off of observed length scales for chemical features seen in the APT data, we can estimate the mean surface diffusivity distance for Cu adatoms during deposition [27]:

$$D_s = \frac{\lambda^2}{2t_d} \quad (1)$$

where D_s is the adatom surface diffusivity, λ is the characteristic adatom diffusion length, and t_d is the deposition time. Despite fast Cu and Nb vapor quench rates found in room temperature deposition [29], surface diffusion rates for Cu and Nb adatoms should be relatively high as they face low diffusion energy barriers on a surface compared to a bulk lattice. To find λ , we can compare this estimated diffusivity to that implied by the size of phase segregated regions in 3D interfaces found by APT. Observed Cu-rich regions are 10 nm wide, which we can take as a characteristic length scale for diffusion. To determine t_d we consider how much time is allotted to an adatom to diffuse on the sample surface before being buried by an atomic monolayer. A Cu atom has 0.69 s to undergo surface diffusion before being buried by a monatomic layer of Cu at a deposition rate of 3 Å/sec. For 40–10 Cu/Nb, this length and time correspond to a surface diffusivity of 3.62×10^{-17} m²/s, which is much faster than the bulk diffusivity of Cu at modestly elevated temperature (2.9×10^{-23} m²/s at 574 K) [30]. We can also compare adatom diffusivity during PVD synthesis of 3D interfaces estimated from our APT measurements to Cu-on-Cu surface diffusivity values. The surface diffusivity of Cu on (111) Cu was found via Monte Carlo simulation [29]

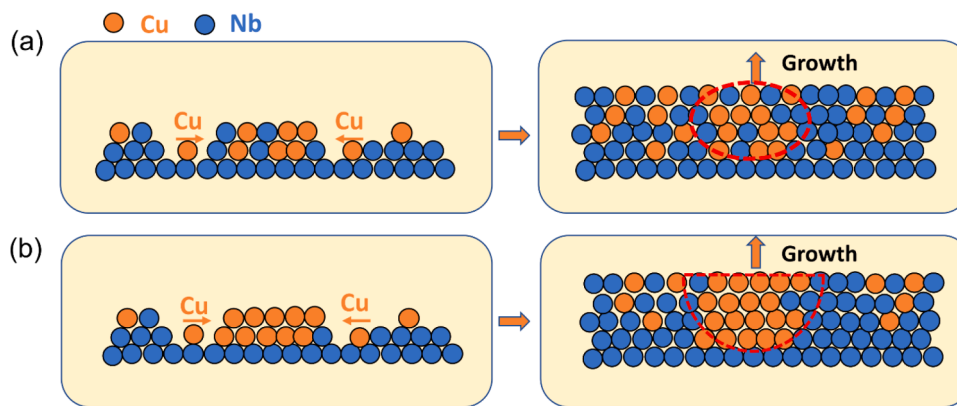


Fig. 5. (a) Schematic of the formation of a Cu-rich region resulting from surface diffusion during PVD. (b) Schematic of the formation of a nearly pure Cu region using similar logic as (a).

to be $2 \times 10^{-10} \text{ m}^2/\text{s}$ and via field ion microscopy [31] to be $8 \times 10^{-8} \text{ m}^2/\text{s}$, both at 300 K. Thus, the estimated surface diffusivity of Cu during deposition of 3D interfaces falls between the values for Cu bulk self-diffusivity and surface diffusivity of Cu on (111) Cu. This suggests that the flux of incoming atoms during deposition hinders surface diffusion, meaning that diffusivity can be tailored by deposition conditions. From Eq. (1), the size of nanoscale features in a PVD-synthesized 3D interface can be tailored if the diffusivity or time allotted for diffusion are altered. This strategy has been used to tailor Cu/Mo and Cu/Ta bicontinuous nanocomposite morphologies by altering substrate temperature and deposition rate, respectively [32,33]. The same outcome can be expected for Cu/Nb, allowing for control of size distribution of both crystallographic and chemical heterogeneities in 3D interfaces.

While our work suggests that crystallographic heterogeneities observed in HRTEM in 3D interfaces correlate with chemical heterogeneities observed in APT, this topic is not fully explored. We studied this partially using molecular dynamics simulations of quenched CuNb melts elsewhere [14], finding that Cu- and Nb-rich compositions favor fcc and bcc structures, respectively, while intermediate compositions favored a completely amorphous structure. However, that study may not fully predict favored metastable structures in PVD-synthesized 3D interfaces; the energy landscape experienced by Cu and Nb adatoms on a planar substrate differs from the landscape encountered in a cooling melt. Similar results have been demonstrated experimentally on cryogenically deposited CuNb alloys, but only explore metastable structure as a function of composition in crystallographically homogeneous systems [34]. A different approach is needed to correlate structural and chemical heterogeneities in 3D interfaces, which we plan to execute using correlative TEM and APT work in the future.

In summary, we have quantified the chemical distribution in 3D for a 3D Cu/Nb interface, established a characteristic length scale of a few nm associated with chemical heterogeneities in Cu/Nb 3D interfaces, and measured interface thickness using APT. These results suggest that 3D interface morphology and crystallography can be tuned by altering PVD deposition speed or substrate temperatures. Alteration of chemical and structural heterogeneities in 3D interfaces likely provides a way to profoundly influence material behavior. Control of 3D interface structure will pave the way for establishment of new interface processing-structure-property relationships in technologically important nanostructured materials.

Declaration of Competing Interest

The authors declare that they have no known competing financial interests or personal relationships that could have appeared to influence the work reported in this paper.

Acknowledgement

This work is supported by DOE BES DE-SC0020133 Office of Science, Basic Energy Sciences. J.Y. Cheng is supported in part by DOE NNSA under cooperative agreement number DE-NA0003960. APT research was supported by the Center for Nanophase Materials Sciences (CNMS), which is a US Department of Energy, Office of Science User Facility at Oak Ridge National Laboratory. The authors would like to thank James Burns for assistance in performing APT sample preparation and running the APT experiments. Samples were synthesized at the Center for Integrated Nanotechnologies, an Office of Science User Facility operated for the U.S. Department of Energy (DOE) Office of Science. Los Alamos National Laboratory, an affirmative action equal opportunity employer, is managed by Triad National Security, LLC for the U.S. Department of Energy's NNSA, under contract 89233218CNA00001. Parts of this work were carried out in the Characterization Facility, University of Minnesota, which receives partial support from the NSF through the MRSEC (Award Number DMR-2011401) and the NNCI (Award Number ECCS-2025124) programs.

Supplementary materials

Supplementary material associated with this article can be found, in the online version, at doi:[10.1016/j.scriptamat.2022.115078](https://doi.org/10.1016/j.scriptamat.2022.115078).

References

- [1] N.A. Mara, I.J. Beyerlein, Curr. Opin. Solid State Mater. Sci. 19 (2015) 265–276.
- [2] M.J. Buehler, A. Misra, MRS Bull. 44 (2019) 19–24.
- [3] A. Sáenz-Trevizo, A.M. Hodge, Nanotechnology 31 (2020), 292002.
- [4] M.J. Demkowicz, P. Bellon, B.D. Wirth, MRS Bull. 35 (2010) 992–998.
- [5] D. Raabe, M. Herbig, S. Sandlöbes, Y. Li, D. Tytko, M. Kuzmina, D. Ponge, P. Choi, Curr. Opin. Solid State Mater. Sci. 18 (2014) 253–261.
- [6] M.A. Meyers, A. Mishra, D.J. Benson, Prog. Mater. Sci. 51 (2006) 427–556.
- [7] K. Lu, L. Lu, S. Suresh, Science 324 (2009) 349–352.
- [8] I.J. Beyerlein, N.A. Mara, J. Wang, J.S. Carpenter, S.J. Zheng, W.Z. Han, R. F. Zhang, K. Kang, T. Nizolek, T.M. Pollock, JOM 64 (2012) 1192–1207.
- [9] N.A. Mara, D. Bhattacharyya, P. Dickerson, R.G. Hoagland, A. Misra, Appl. Phys. Lett. 92 (2008), 231901.
- [10] N.A. Mara, D. Bhattacharyya, J.P. Hirth, P. Dickerson, A. Misra, Appl. Phys. Lett. 97 (2010), 021909.
- [11] M.J. Demkowicz, R.G. Hoagland, J. Nucl. Mater. 372 (2008) 45–52.
- [12] K. Yu-Zhang, J.D. Embury, K. Han, A. Misra, Philos. Mag. 88 (2008) 2559–2567.
- [13] Y. Chen, N. Li, R.G. Hoagland, X.-Y. Liu, J.K. Baldwin, I.J. Beyerlein, J.Y. Cheng, N. Mara, Acta Mater. 199 (2020) 593–601.
- [14] S. Xu, J.Y. Cheng, Z. Li, I.J. Beyerlein, N.A. Mara, Comput. Methods Appl. Mech. Eng. 389 (2022), 114426.
- [15] J.Y. Cheng, S. Xu, Y. Chen, Z. Li, J.K. Baldwin, I.J. Beyerlein, N.A. Mara, Nano Lett. 22 (2022) 1897–1904.
- [16] C.B. Carter, D.B. Williams, Transmission Electron Microscopy: Diffraction, Imaging, and Spectrometry, Springer, 2016.
- [17] J.D. Poplawsky, W. Guo, N. Paudel, A. Ng, K. More, D. Leonard, Y. Yan, Nat. Commun. 7 (2016) 12537.

- [18] F. Vurpillot, A. Cerezo, D. Blavette, D.J. Larson, *Microsc. Microanal.* 10 (2004) 384–390.
- [19] M.K. Miller, M.G. Hetherington, *Surf. Sci.* 246 (1991) 442–449.
- [20] K. Thompson, D. Lawrence, D.J. Larson, J.D. Olson, T.F. Kelly, B. Gorman, *Ultramicroscopy* 107 (2007) 131–139.
- [21] D.J. Larson, D.T. Foord, A.K. Petford-Long, A. Cerezo, G.D.W. Smith, *Nanotechnology* 10 (1999) 45–50.
- [22] J.Y. Hwang, S. Nag, A.R.P. Singh, R. Srinivasan, J. Tiley, H.L. Fraser, R. Banerjee, *Scr. Mater.* 61 (2009) 92–95.
- [23] M. Atzmon, D.A. Kessler, D.J. Srolovitz, *J. Appl. Phys.* 72 (1992) 442–446.
- [24] P.B. Barna, M. Adamik, *Thin Solid Film.* 317 (1998) 27–33.
- [25] A. Anders, *Thin Solid Film.* 518 (2010) 4087–4090.
- [26] Y. Cui, B. Derby, N. Li, A. Misra, *Mater. Des.* 166 (2019), 107602.
- [27] B.K. Derby, A. Chatterjee, A. Misra, *J. Appl. Phys.* 128 (2020), 035303.
- [28] I.E. Bauer, *Z Krist* 110 (1958) 372–394.
- [29] P.M. Agrawal, B.M. Rice, D.L. Thompson, *Surf. Sci.* 515 (2002) 21–35.
- [30] K. Maier, *Phys. Status Solidi* 44 (1977) 567–576.
- [31] A. Kapoor, R.T. Yang, C. Wong, *Catal. Rev. 31* (1989) 129–214.
- [32] Y. Cui, B. Derby, N. Li, N.A. Mara, A. Misra, *Mater. Res. Lett.* 6 (2018) 184–190.
- [33] M. Powers, B. Derby, A. Shaw, E. Raeker, A. Misra, *J. Mater. Res.* 35 (2020) 1531–1542.
- [34] E. Ma, *Prog. Mater. Sci.* 50 (2005) 413–509.